Electrical Engineering in Japan, Vol. 75, No. 3, 1975
Translated from Denki Gakkai Ronbunshi, Vol. 95A, No. 5, May 1975, pp. 187-193

Dielectric Properties of Inorganic Salts (KNO_2, $NaNO_2$, $CaCO_3$) under High Pressure by Liquid-Solid Hybrid Systems

S. FUJIMOTO and N. YASUDA
Electrical Engineering Department, Gifu University
M. KOIZUMI
Institute of Scientific and Industrial Research, Osaka University

1. Introduction

Because of the difficulty in applying the static pressure on the sample and also because of the fragility of the sample itself, the physical properties of solid materials have been investigated by high-pressure apparatus [1, 2] employing gas or liquid media which can withstand higher pressure than solid media.

The liquid-media, tapered-cylindrical, high-pressure apparatus which was developed by Bridgman and later improved by Birch produces the pressure up to 20 kbar and suffers from a crack of the cylinder wall if higher pressure is required.

We have developed a liquid-solid hybrid system which was first proposed by Barett [4], and measured dielectric properties of salts (KNO_2, $NaNO_2$ and $CaCO_3$) under high pressure up to 40 kbar at 100 kHz. It was found that the permittivity increases with the pressure and the logarithmic dielectric conductivity decreases in an inverse proportion to the pressure.

This paper reports the construction of a liquid-solid hybrid high-pressure apparatus and presents the experimental results on the dielectric properties of salts under high pressure. So far, no papers have reported the pressure dependence of the permittivity of salts except Rochelle salts [2], barium titanate [5] and nitric soda [6].

2. Sample and High-Pressure Device

2.1 Selection of samples

A number of papers has reported ferroelectric behaviors of inorganic salts which change their center-symmetric phase at transition temperature. However, the effect of high pressure on their ferroelectric behaviors is not well known.

Under high pressure, some salts exhibit ferroelectric properties after the transition from center-symmetric phase to noncenter-symmetric phase. Other salts reveal ordinary electric properties after the transition from noncenter-symmetric phase to center-symmetric phase. The former includes $NaK\,C_4H_4O_6 \cdot 4\,H_2O$ (Rochelle salt), $NaNO_3$ [6], etc., while the latter includes $BaTiO_3$, KH_2PO_4, $LiH_3(SeO_3)_2$ (lithium hydroxide in selenious acid), etc.

Based on data of crystalline symmetry in the X-ray diffraction measurement, the temperature versus pressure diagram in the thermal analysis, and anomalous permittivity in the dielectric measurement, we selected ClO_3, NO_2, NO_3, SO_4, CrO_4, etc. Further, eliminating absorptive, unstable and low-conductivity samples, we finally selected three kinds of inorganic salts, i.e., KNO_2, $NaNO_2$ and $CaCO_3$.

2.2 Sample preparation

(1) KNO_2

The 85% KNO_2 powder was refined from the solution by the recrystallization method. The KNO_2 powder thus obtained was poured into a shaping machine with the mirror surface polished by No. 1500 Al_2O_3 powder to form a disk (thickness 0.7 mm, and diameter 10 mm) under the pressure of 1500 kg/cm^2. The silver paste applied to the disk surface was used as an electrode.

Since KNO_2 is highly sensitive to moisture, the sample was kept in a high-temperature bath for one day and then yellow wax was applied to its surface to protect the sample from moisture penetration.

(2) $NaNO_2$

The 98% $NaNO_2$ powder was poured into a pyrex glass crucible (inner diameter 2.3 cm and length

17 cm). The crucible was then placed into a furnace at 300°C (melting point 276.9°C) for two days. The temperature was decreased to 188°C at a rate of 0.76°C/h. The temperature was further decreased to 130°C at a rate of 1.02°C/h near the Curie point (163.3°C). Below 130°C, the sample was cooled naturally until $NaNO_2$ crystal was produced. The ingot of this crystal was cleaved. There the crystal was cut in the direction normal to the b-axis by use of a wet string inserted into a {1, 0, 1} cleavage. The plate with an area of 30 to 40 mm^2 was then carefully hand-lapped until its thickness reached 0.20 mm by using No. 1500 Al_2O_3 powder containing alcohol. Then the disk was dried in the 100°C temperature bath and was applied by silver paste as an electrode. The sample thus obtained was b-plate.

(3) $CaCO_3$

Since $CaCO_3$ has a very high melting point, single crystals of natural calcite were used. After it was confirmed by polarizing microscope that the crystal was clean it was cut in the direction normal to the c-axis using a cleaved surface and then hand-lapped by using No. 1500 Al_2O_3 powder until the thickness became 0.16 mm. The sample thus produced has an area of 40 to 50 mm^2.

2.3 High-pressure apparatus

We have constructed a high-pressure apparatus employing a liquid-solid hybrid system using tungsten carbide. The high-pressure apparatus which is capable of producing above 20 kbar must meet the following conditions:

(a) The lead wires connecting the sample and Q meter via gaskets must not maintain high resistivity against high pressure. Further, the stray capacitance between wires must be constant.

(b) The pressure cells must be constructed such that the liquid medium is completely shielded.

(c) The gasket at the lead-wire outlet must have sufficient viscosity such that the lead wire is not disconnected.

In the following are described two types of high-pressure apparatus, i.e., type a (Fig. 1) and type b (Fig. 3). Table 1 summarizes the features of these apparatus.

(1) Type-a apparatus

Tungsten-carbide anvils are attached to the ends of each ram of a cubic press which can withstand the maximum pressure of 600 t. The anvil surface is a square with a 20-mm side and presses each of 6 surfaces of the pressure cell. As seen in Fig. 1, the pressure cell is a cubic pyrophyllite (② 23 mm in side length) with fin-shaped pregaskets in which a vaseline-filled cylindrical capsule is inserted. The capsule is composed of a stainless steel body ③ and a cap ①.

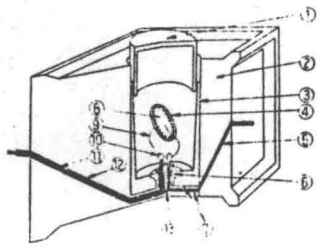

① Capsule, ② Cubic pyrophyllite, ③ Capsule body, ④ Sample, ⑤ Copper wire, ⑥ Pyrophyllite cone, ⑦ Thin pyrophyllite plate, ⑧ Electrode, ⑨ Enamel lead wire, ⑩ Soldering, ⑪ Nichrome wire, ⑫ Teflon tube, ⑬ Epoxy resin.

Fig. 1. Main part of type-a high pressure apparatus.

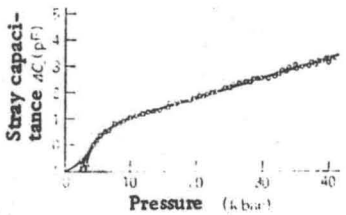

Fig. 2. Pressure dependence of stray capacitance ΔCs of positive lead.

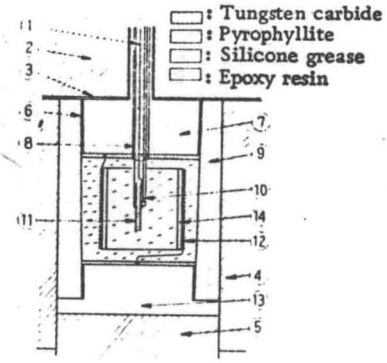

① Al_2O_3 ceramic insulating tube, ② End plate, ③ Mica plate ④ Pressure vessel (cylinder), ⑤ Pressure vessel (piston), ⑥ Lead foil, ⑦ Upper cap, ⑧ Enamel wire, ⑨,⑩ Pyrophyllite cylinder, ⑭ Alumel-chromel thermocouple, ⑪ Sample ⑫ Manganin winding, ⑬ Lower cap.

Fig. 3. Main part of type-b pressure apparatus (under high pressure).

(i) The inner and outer diameters of the capsule body are 12 and 13 mm, respectively, and the capsule length and inner depth are 18 and 15 mm, respectively. The capsule inner wall is tapered at 1° with respect to the axial direction. (ii) The inner and outer diameters are 11 and 12 mm and the capsule length and depth are 9 and 8 mm, respectively.

Table 1. Characteristics of high-pressure apparatus of type a and type b

Types	Method	Pressure limit	Effective volume	Press	Temperature controller	Pressure cell
Type a	Multianvil system; the area of anvil tip is 20 x 20 mm^2	Because of the principle of massive support, the pressure (4.5 ~ 40 kbar) higher than the withstand pressure of tungsten·carbide can be obtained	$\pi x(11/2)^2$ x13 mm^3	Six 600-t cubic presses	Yes	complicated (Fig. 1)
Type b	Piston cylinder system; cylinder metal diameter is 20 mm	The pressure range is limited to 0 ~ 30 kbar because of the withstand pressure of tungsten·carbide which forms a high-pressure vessel	$\pi x(12/2)^2$ x18 mm^3	500-t Kennedy dual presses	No	simple (Fig. 3)

Lead foils are attached around the capsule cap to shield the vaseline as well as to facilitate smooth insertion of the cap into the capsule body.

Vaseline (fluid pressure medium) allows one to apply the same static pressure as oil. Even a fragile crystal plate 0.16 mm in thickness can be tested without damage by applying high pressure.

When a cubic press is used, one of the sample electrodes is connected to the ground via one of the anvils and the other electrode is connected to ⊕ terminal of the meter via one of the anvils. In our experiment, one of the electrodes ⑧ of the sample ④ is grounded together with all anvils via 0.3 mm-diameter copper wires imbedded in pyrophyllite. The other electrode is connected to the ⊕ terminal of the meter via gaskets using 0.5 mm-diameter nichrome wire ⑪ covered by a Teflon tube ⑫ which can reduce stray capacitance and leakage conductance. Nichrome wires can withstand a large tensile stress.

Below 4.5 kbar gaskets are not effectively formed in the pressure cell and unstable pressure is applied to the sample. The stray capacitance due to the pressure varies from cell to cell, and therefore, no dielectric measurement was made below 4.5 kbar.

Figure 2 shows the pressure dependence of stray capacitance of the positive lead wire in the apparatus without the sample. The variation of the stray capacitance ΔC_S increases with the pressure. When the sample is inserted into the apparatus, the variation of the effective stray capacitance of the sample is evaluated as $\Delta C - \Delta C_S$, where ΔC is the capacitance of the sample including the stray capacitance of the lead wire.

Denoting by C_0 the capacitance of the sample at the atmospheric pressure, and by ε_{r0} specific permittivity, the specific permittivity of the sample at the pressure p (kbar) above 4.5 kbar is

$$\tau\varepsilon_{rp} = \varepsilon_{r4.5} + \varepsilon_{r0}\Delta C_n/C_0$$

where $\varepsilon_{r4.5}$ is the specific permittivity at 4.5 kbar, m is the material constant and τ is the correction factor of the capacitance

$$\tau = 1 - mp$$

where m = 3.0 x 10^{-4}/kbar for crystal and 7.5 x 10^{-4}/kbar for powder [8].

(b) Type-b, high-pressure apparatus

A cylindrical pressure cell is placed inside a pressure vessel to which pressure is applied by a Kennedy-type 500 t press (see Fig. 3). The cell consists of a pyrophyllite cylinder ⑨ (o.d. 20 mm, i.d. 13.2 mm and length 28 mm) with both ends covered by steel caps ⑦ and ⑬. The cell is filled with silicon grease in which sample ⑩ is imbedded. The inner wall of the cell is tapered at 1° along the axis. The lead foil ⑥ is attached on the contacts between the cell inner walls and caps. This foil facilitates realizing good contact between the cell and caps when high pressure is applied to caps via the pressure vessel.

An Al_2O_3 insulating tube (dia. 2 mm) ① is inserted into the sample cell via four holes (dia. 0.4 mm) of the upper cap ⑦. This tube contains a pair of enamel copper wires which connect a thermocouple ⑩ on the sample surface to the microvolt meter. Gaps between the holes and two pairs of lead wires and between the holes and the insulating tube are filled by epoxy resin to shield the silicon grease.

Manganin-wire coil ⑫ is installed on the inner wall of pyrophyllite cylinder ⑭ inside a cell to control the sample temperature. The lead wires are connected to the upper and lower caps which supply power to the wires. The pressure vessel ⑤ and end plate ② are electrically insulated by use of mica plate ③.

The oil pressure was corrected on the basis of the principle that electrical resistance changes rapidly at the phase transition points I-II (25.5

kbar) and II-III (27.0 kbar) of bismuth and I-II (37.0 kbar) of thallium.

3. Experimental Results

The capacitance C and loss tangent tan δ was measured by Q-meter at 100 kHz in the pressure range of 0 to 40 kbar. The spontaneous polarization was measured by the improved Sawyer-Tower circuit [9]. The type-a apparatus was used for the measurement of the phases I and II of $CaCO_3$ and type-b for other measurements.

3.1 Dielectric properties of KNO_2

Previously, we reported that KNO_2 is not ferroelectric at room temperature and its permittivity is invariant of the pressure at phase II [7]. Figure A1 shows the temperature-pressure phase diagrams [10] of KNO_2. Figure 4 shows the pressure dependence of logarithmic dielectric conductivity ($\log_e \omega_\varepsilon \tan\delta$) at $\omega = 2\pi \times 10^5$. At a constant temperature, $\log_\varepsilon \sigma$ decreases linearly with p

$$\log_e \sigma = -\alpha p + \log_e \sigma_0 \qquad (1)$$

where $\alpha = d \log \cdot \sigma / dp$ represents a gradient of the linear portion and is a constant independently of the pressure, and σ_0 is the dielectric conductivity at zero pressure.

At the temperature T(K), electrical conductivity σ of ionic crystal is given by

$$\log_e \sigma = -E/kT + \log_e \phi/kT \qquad (2)$$

where E is the activation energy, U is energy in the diffusion of lattice defects in the crystal and W is the energy in the generation of lattice defects, where E = U + W/2 (intrinsic region) and E = U (extrinsic region), k is the Boltzmann constant, and ϕ is a constant which is determined by the crystal itself.

Recently, Samara reported that logarithmic dielectric conductivity of thallium halogenide decreases with an inverse of the absolute temperature at low frequencies of 1 to 100 kHz under constant pressure. In addition, he pointed out that Eq. (2) holds even at the dc and low frequencies; activation energy obtained from the straight portion of the characteristic curves agrees with that obtained from the measurement of ionic conduction [11].

Substituting empirical Eq. (1) into Eq. (2), we obtain

$$E = \beta p + E_0 \qquad (3)$$

where

$$\beta = \alpha kT,\ E_0 = kT \log_e (\phi / kT\sigma_0)$$

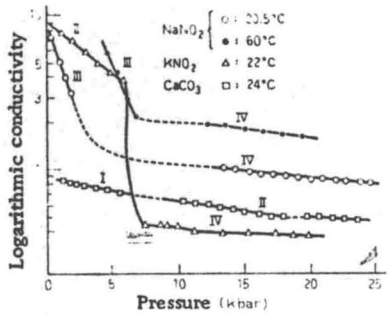

Fig. 4. Pressure dependence of logarithmic dielectric conductivity ($\log_e \sigma$) of a c-plate $CaCO_3$ (24°C), powdered KNO_2 (22°C) and a b-plate $NaNO_2$ (20.5°C, 60°C). $\varepsilon_r = 12.7$ and $\tan\delta = 0.55$ under atmospheric conditions for KNO_2 (100 kHz).

Therefore, activation energy increases in proportion to the pressure at a constant temperature. From the mark Δ in Fig. 4, we obtain $\beta = dt/dp = 4.1 \times 10^{-3}$ eV/kbar in phase II at the transition pressure less than 6.4 kbar. Electrical conductivity of KNO_2 at room temperature under normal pressure is in the intrinsic region and its activation energy is 0.63 eV [12]. Therefore at high pressure, the activation energy exceeds 0.63 eV.

The above-mentioned facts can be explained as follows; under high pressure, crystals are pressurized and the diffusion and generation of lattice defects cease. As a result, both U and W/2 increase and electrical conductivity decreases. Therefore, the effect of the pressure increase on electrical conduction is similar to the effect of the temperature reduction on the electrical conduction. In Samara's experiment under normal pressure, the temperature dependence of $\log_e \sigma$ is very small below 290 K. In Fig. 4 the pressure dependence of $\log_e \sigma$ is small at high pressure.

3.2 Dielectric properties of $NaNO_3$

Since Sawada's discovery of ferroelectric properties of $NaNO_2$ in 1958 [13], a number of researchers has reported that the phase I is ordinarily dielectric, phase II is anti-ferroelectric, and phase III is ferroelectric. The phase diagram is shown in Fig. 7 A2 [10]. However, no one has reported the phase transition from the phase III to IV and the dielectric properties at the phase IV.

Figure 5 shows the pressure dependence of permittivity and loss tangent of b-plate $NaNO_2$ at 100 kHz.

(i) The pressure corresponding to the III-IV phase transition is 8.7 kbar at 20.5°C and 11.0 kbar at 60°C. The relative permittivity is constant at the phase III, and decreases rapidly by

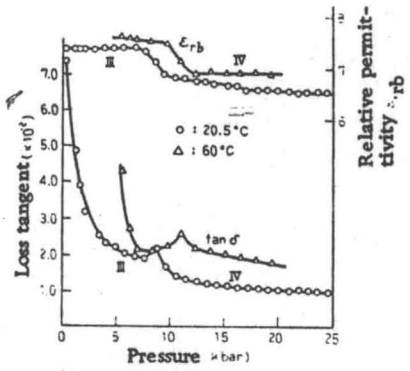

Fig. 5. Pressure dependence of relative permittivity (ε_{rb}) and loss tangent (tan δ) of a b-plate $NaNO_2$ at 100 kHz (20.5°C, 50°C).

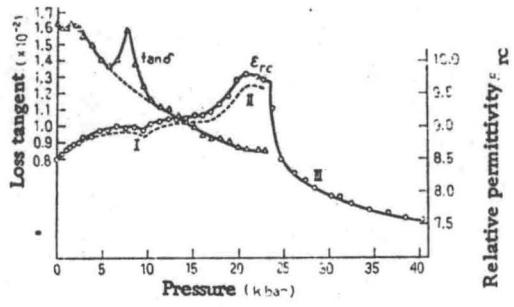

Fig. 6. Pressure dependence of relative permittivity (ε_{rc}) and loss tangent (tan δ) of a c-plate $CaCO_3$ at 100 kHz (24°C).

68% at the III-IV phase-transition pressure and then becomes constant at the phase IV.

(ii) The loss tangent exhibits small peaks at the III-IV phase transition pressure.

(iii) With increasing temperature, the pressure versus permittivity curve and the pressure versus loss tangent curve shift toward the high-pressure side.

A set of the transition pressures (8.7 kbar, 11.0 kbar) shown in Fig. 6 agrees with the transition pressure obtained by Rapoport [10] and Bridgman [14] by the volume-discontinuity method [see Fig. 7 (A2)].

The reduction of permittivity and the occurrence of small peaks of loss tangent at the transition pressure may be due to dispersion effect caused by jumping of ions to empty lattices under electric field.

The marks O and ● represent the pressure dependence of $\log_e \sigma$ which are obtained from ε_{rb} and tan δ in Fig. 5. As seen in these curves at low pressures (below 2 kbar at 20.5°C and below 7.0 kbar at 60°C) and in the phase IV, the value of $\log_e \sigma$ decreases with the pressure p according to Eq. (1). Its pressure dependence is expressed as $\beta = 1.30 \times 10^{-2}$ eV/kbar (20.5°C) and 1.35×10^{-2} eV/kbar (60°C) in phase III and 6.0×10^{-4} eV/kbar (20.5°C) and 6.3×10^{-4} eV/kbar (60°C) in the phase IV. The pressure dependences of activation energy in both phases differ, but activation energy increases with the pressure. The electrical conduction of $NaNO_2$ is in the intrinsic region at room temperature under normal pressure.

When electric field of 1.1×10^6 V/m was applied to the sample under the pressure of 15 kbar, hysteresis loops were observed in the field vs. flux density characteristic curves at the temperature above 123°C. This indicates that the sample is ferroelectric in phase III above 123°C and its spontaneous polarization is 0.3 $\mu C/cm^2$.

3.3 Dielectric properties of $CaCO_3$

The physical properties of $CaCO_3$ under high pressure have been investigated by Bridgman's volume-discontinuity method [15], Davis' X-ray diffraction method [16] and Bell's D.T.A. method [17]. Figure 7 (A3) shows the phase diagram of $CaCO_3$ [18].

Figure 6 shows the pressure dependence of permittivity and loss tangent of a c-plate $CaCO_3$. From this figure, we conclude that:

(i) The permittivity increases gradually with the pressure in the pressure range from 0 to 18 kbar and increases rapidly near 18 kbar and becomes constant in the region II (19 to 23 kbar) and then decreases in the region III (above 23 kbar).

(ii) The loss tangent curves exhibit peaks at 8 kbar.

The above regions I, II and III correspond to the phases I, II and III of $CaCO_3$. The transition pressure (19 kbar, 23 kbar) obtained in this experiment at room temperature is slightly higher than the transition pressures (14.6 kbar, 17.7 kbar) obtained by the volume-discontinuity method [15] and (15.5 kbar, 18.7 kbar) obtained by X-ray diffraction method [16].

According to the conventional studies on the pressure dependence of the permittivity of solid materials at low frequencies, the permittivity decreases with the pressure. Mayburg reported that the permittivity of ionic crystals, such as MgO, LiF, NaCl, KCl, etc., decrease with the pressure at 1 kHz. He stated that this permittivity reduction is due to an increase of repulsion among ions which decreases the polarization coefficient and also due to overlapping of neighboring ions which decreases an internal electric field [19].

Unlike Mayburg's results, the permittivity of $CaCO_3$ in the phase I obtained in this measurement increases with the pressure. This may be due to the following reasons: with an increase of

the pressure, the sample density and dipole moment increase, resulting in an increase of the permittivity.

The dotted line in Fig. 6 represents the permittivity obtained by Davis' X-ray diffraction method with the correction made with consideration of the sample deformation. Davis pointed out that the phase V of $CaCO_3$ is characterized by the same calcite-type hexagonal pseudo cells as in the X-ray diffraction pattern for the phase III of KNO_3, because the phase diagram of $CaCO_3$ is similar to that of KNO_3. He also concluded that the phase II of $CaCO_3$ has the same structure as the phase III of KNO_3 [16]. It is also confirmed that the phase III of KNO_3 is ferroelectric [1].

We have measured the field vs. flux density relation for the phase II of $CaCO_3$ at room temperature. However, no hysteresis loops appeared and no spontaneous polarization was observed. Further, the permittivity does not exhibit peaks at the transition pressure. Therefore, it is concluded that $CaCO_3$ is not ferroelectric in the phase II, and is different from KNO_3 in the phase III.

As seen in Fig. 6, the loss tangent exhibits a peak at 8 kbar in the phase II under room temperature. The permittivity also varies slightly near this peak. This variation may be due to new phase transition.

Marks □ in Fig. 4 represent the pressure dependence of $\log_e \sigma$ which is obtained from ε_{rc} where the effect of abnormal peaks of loss tangent on ε_{re} is not considered. As seen in this figure, $\log_e \sigma$ of $CaCO_3$ in the phases I and II decreases linearly with the pressure according to Eq. (1). The activation energy per unit pressure is 9.0×10^{-4} eV/kbar at low pressure (below 8 kbar) in the phase I, 8.5×10^{-4} eV/kbar at high pressure (above 8 kbar) and 30×10^{-4} eV/kbar in the phase II.

At room temperature under normal pressure, electrical conduction in $CaCO_3$ takes place in extrinsic region. Its activation energy is 0.11 eV [20] and increases further with an increase of the pressure.

4. Conclusions

According to the previous studies, the permittivity of solid materials decreases with an increase of the pressure because of the reduction of the polarization coefficient due to limited ionic motion. However, our experimental results indicate that the permittivity of $CaCO_3$ in the phase I increases with the pressure.

The logarithmic dielectric conductivity at low frequencies decreases linearly with an increase of the temperature. This phenomenon is related to the diffusion (or generation) of lattice defects and can be explained as an increase of activation energy with the pressure.

The pressure dependence of the conductivity dE/dp decreases gradually with the pressure. The values of dE/dp of KNO_2, $NaNO_3$ and $CaCO_3$ are almost identical to those of KCl and KBr [21].

APPENDIX

Figure A1(a) [10], (b) [10] and (c) [18] show the temperature-pressure phase diagrams of KNO_2, $NaNO_2$ and $CaCO_3$ which were obtained by Rapoport. These figures also include our test results marked by —·— or O.

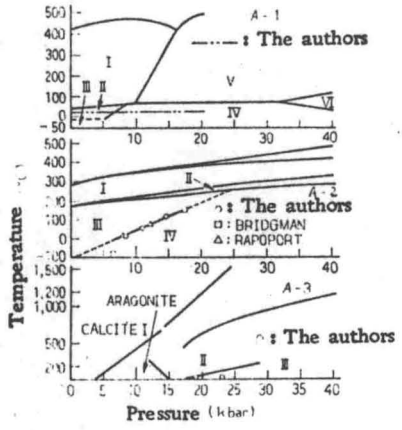

Fig. A1. Temperature-pressure phase diagrams for KNO_2 (A-1), $NaNO_3$ (A-2) and $CaCO_3$ (A-3) (after Rapoport).

REFERENCES

1. M. Midorikawa, Y. Ishibashi and Y. Takagi. J. Phys. Soc. Japan, Vol. 30, 449, 1971.
2. G.A. Samara. J. Phys. Chem. Solids, Vol. 26, 121, 1965.
3. F. Birch, E.C. Robertson and S.P. Clark. Indust. Engr. Chem., Vol. 49, 1965, 1957.
4. J.D. Barnett and C.D. Bosco. Rev. Sci. Instrum., Vol. 38, 957, 1967.
5. G.A. Samara. Advances in High Pressure Research 3, p. 174, Academic Press, 1969.
6. Fujimoto, J.D. Barnett. Trans. I.E.E., Japan, Vol. 93-A, 8, 1973.
7. S. Fujimoto, N. Yasuda, M. Koizumi and M. Shimada. Japan J. Appl. Phys., Vol. 13, 735, 1974.
8. J.D. Barnett, J. Pack and H.T. Hall. Trans. Amer. Cryst. Assoc., Vol. 5, 113, 1963.
9. Y.T. Tsui, P.D. Hinderaker and F.J. McFadden. Rev. Sci. Instrum., Vol. 39, 1423, 1968.

10. E. Rapoport. J. Chem. Phys., Vol. 15, 2721, 1966.
11. G.A. Samara. Phys. Rev., Vol. 165, 959, 1968.
12. A. Mansingh and A.M. Smith. J. Phys. D., p. 560, 1971.
13. S. Sawada, S. Nomura, S. Fuji and J. Yoshida. Phys. Rev. Letters, Vol. 1, 320, 1958.
14. P.W. Bridgman. Proc. Amer. Acad. Arts Sci., Vol. 72, 45, 1937.
15. P.W. Bridgman. Amer. J. Sci., Vol. 273, 7, 1939.
16. B.L. Davis. Sci., Vol. 31, 489, 1964.
17. P.M. Bell and J.J. England. Carnegie Inst. Washington, Publ. Geophys. Lab., Vol. 63, 176, 1964.
18. E. Rapoport. J. Phys. Chem. Solids, Vol. 27, 1349, 1966.
19. S. Mayburg. Phys. Rev., Vol. 79, 375, 1960.
20. K.S. Rao and K.V. Rao. Zeit. Physik, Vol. 216, 300, 1968.
21. D.N. Yoon and D. Lazarus. Phys. Rev., Vol. 5, 4935, 1972.

Submitted August 9, 1974;
resubmitted December 23, 1974